Available online at www.sciencedirect.com
ScienceDirect
Trans. Nonferrous Met. Soc. China 35(2025) 2148−2163
Transactions of Nonferrous Metals Society of China
www.tnmsc.cn

Effect of Ce element content on microstructure and corrosion resistance of highly-alloyed Al−Zn−Mg−Cu−Zr−Ti alloy

Chen LI, Yun-tian LUO, Qing-shan ZHOU, Meng-nan HAN, Shao-hui SHA, Xiao-jing XU

Institute of Advanced Manufacturing and Modern Equipment Technology, Jiangsu University, Zhenjiang 21200, China

Received 24 November 2023; accepted 2 July 2024

Abstract: To effectively improve the corrosion resistance of aluminum alloys without affecting their strength, the effect of Ce content on the microstructure, stress corrosion, intergranular corrosion, and exfoliation corrosion resistances of Al−11.3Zn−3.1Mg−1.2Cu−0.2Zr−0.1Ti alloy was investigated. The results showed that the addition of Ce formed the $(Zn,Al,Cu)_{22}Ce_3$ phase with a size of 100 nm, which enhanced the recrystallization resistance of the alloy, increased the number of low-angle grain boundaries and dislocation density, refined the grains, promoted the phase transition from GP zone to η' phase, and promoted the size and discontinuity of precipitates at grain boundaries. All Ce-added alloys exhibited the higher resistance to corrosion. The alloy with 0.15 wt.% Ce possessed the optimal corrosion resistance along with the strength and elongation at slow strain rate of 744.8 MPa and 4.6%, respectively, in 3.5 wt.% NaCl solution. The minimum depth of intergranular corrosion and exfoliation corrosion was achieved as well.

Key words: Al−Zn−Mg−Cu alloy; microalloying; stress corrosion cracking; exfoliation corrosion; intergranular corrosion

1 Introduction

Due to its lightweight, high strength, and fatigue-resistant properties, the 7000 series aluminum alloy is extensively applied in modern aerospace and automotive industries [1,2]. The vigorous development of high-performance aluminum alloys with low production costs contributes to achieving lightweight design and enhancing maneuverability in vehicles. Classical melting and casting (also known as "melt casting") is the predominant method for producing Al alloys due to its economic advantages and suitability for industrial production. Hence, an urgent breakthrough is needed in the preparation of ultra-high strength, high toughness, and corrosion-resistant Al alloys based on the melt casting method.

XU et al [3] and CAI et al [4] conducted the in-depth research on the 800 MPa-grade-strength aluminum alloys through composition design and heat treatment. Their findings revealed that the ultra-high strength alloys possessed a high alloying (w(Zn)+w(Mg)>13%) degree to obtain abundant precipitation after aging, resulting in a notable strengthening effect. Nevertheless, a multitude of coarse intermetallic compounds (IMCs) are inevitably produced during the melt casting of the highly-alloyed Al alloy. These coarse IMCs serve as the site for early cracking under the action of strain. Additionally, the existence of the coarse undissolved phases significantly impairs the corrosion resistance in certain environments, particularly for environmentally-assisted cracking (known as stress corrosion cracking, SCC), thereby restricting the alloy's applicability.

The improvement of the strength, ductility,

Corresponding author: Xiao-jing XU, Tel: +86-511-88792058, E-mail: yjs_xx@126.com
https://doi.org/10.1016/S1003-6326(25)66806-3

toughness, and corrosion resistance in alloys can be attained through the addition of trace alloying elements, such as La [5], Er [6,7], Ce [8], and Sc [9]. Among them, the introduction of cost-effective Ce during the melting process is proved to be a valuable method for enhancing the melt quality, modifying the microstructure, and reducing the grain size, which enhances the overall mechanical properties of the alloys. According to the previous research [10], the addition of an appropriate quantity of Ce to aluminum alloys prompts the formation of the Al_4Ce phase. Furthermore, Ce-containing particles hinder the movement of dislocations and grain boundary migration during the recrystallization, resulting in grain refinement of the alloy. HU et al [11] also believe that the $(Al,Zn)_4Ce$ dispersed particles formed by adding 0.04 wt.% Ce in Al−Zn−Mg alloy effectively pin dislocations and grain boundaries, stabilize the substructure of the deformed matrix, suppress the recrystallization nucleation, and enable to achieve the refined subcrystals. The Al−Ce alloy is expected to develop into a high temperature-resistant Al alloy, primarily due to reinforcement provided by $Al_{11}Ce_3$ particles [12]. The presence of $Al_{11}Ce_3$ particles in Al−Ce-based alloys ensures good mechanical properties under both room temperature and high-temperature conditions [13]. In addition, Ce forms a highly-stable oxide, decreasing the surface reactivity and the likelihood of corrosion of the alloy [11]. Therefore, Al−Zn−Mg−Cu alloys are expected to possess enhanced corrosion resistance without losing strength.

In this study, a novel highly-alloyed Al−11.3Zn−3.0Mg−1.2Cu−0.2Zr−0.1Ti−0.01Sr alloy with different contents of Ce was produced using the standard melt casting. The effect of Ce content on the microstructure and corrosion resistance of the highly-alloyed Al−Zn−Mg−Cu alloy was systematically studied. The aim of this work is to develop the aluminum alloy with ultra-high strength and excellent corrosion resistance, establishing the foundation for further optimizing the comprehensive properties of aluminum alloy.

2 Experimental

2.1 Alloy preparation

In the melting and casting process, the pure Al, Al−50.12%Cu intermediate alloy, Al−4.11%Zr intermediate alloy, Al−9.89%Sr intermediate alloy, and Al−5.11%Ti−1%B intermediate alloy were placed in a crucible. The crucible was then placed in a well furnace heated to 900 °C and held for 1.5−2 h. Then, the furnace was cooled to 750 °C and refined with the hexachloroethane refining agent (C_2Cl_6). After refining, the pure Mg and Zn (99.9%) were added, and the melt was stirred. Subsequently, a secondary refining with the hexachloroethane refining agent (C_2Cl_6) was conducted and held for 15 min. The Al−10%Ce intermediate alloy was added to the melt, and the slag was removed after standing for 15 min. Finally, the melt was poured into the preheated 400 °C cast iron mold. The actual compositions of the produced alloys were determined by the spectrometer (Table 1) at Ce contents of 0, 0.15, 0.3, and 0.45 wt.%. According to their compositions, the samples were labeled as 0-Ce, 0.15-Ce, 0.3-Ce, and 0.45-Ce, respectively.

Table 1 Measured compositions of aluminum alloy samples (wt.%)

Sample	Zn	Mg	Cu	Sr	Zr	Ti	Ce	Al
0-Ce	11.2	3.1	1.21	0.015	0.265	0.131	0	Bal.
0.15-Ce	11.7	3.05	1.28	0.016	0.249	0.116	0.15	Bal.
0.3-Ce	11.3	3.09	1.21	0.019	0.211	0.123	0.30	Bal.
0.45-Ce	11.3	2.95	1.15	0.013	0.279	0.132	0.45	Bal.

The homogenization process was performed as a single-stage heat treatment (450 °C for 24 h, followed by cooling in the furnace). Subsequently, the homogenized ingots were hot-extruded into 10 mm diameter rods with an extrusion ratio of 10:1 at a speed of 10 mm/s at 400 °C. The next step was the solid solution treatment ((450 °C, 2 h) + (460 °C, 3 h) + (470 °C, 1.5 h) (water quenching)), after which the samples underwent aging at 120 °C for 24 h.

2.2 Microstructural characterization

The tensile fractures of specimens were characterized using the JEOL−IT300 scanning electron microscope (SEM) equipped with an energy dispersive spectrometer (EDS). For the evaluation of the crystal structure of the solid solution alloys, an EDAX Velocity Super type electron backscatter diffraction (EBSD) was employed, and the tested surface was orientated

perpendicular to the extrusion direction (ED). In the obtained EBSD results, the grain boundaries with misorientation angles greater than 15° were classified as high-angle grain boundaries (HAGBs), while those with misorientation angles between 2° and 15° were referred to as low-angle grain boundaries (LAGBs). The grain orientation spread (GOS) represents the average deviation in orientation between each point in the grain and the average orientation of the grain, where the recrystallized grain is expected to exhibit the GOS value of less than 3° [14]. The samples were collected from the centers of the aged alloy rods (perpendicular to the ED) and analyzed using the Talos F200X high-resolution transmission electron microscopy (HRTEM). Subsequently, the TEM specimens underwent mechanical thinning, followed by twin-jet electropolishing at −25 °C using a solution comprising 70 vol.% methanol and 30 vol.% nitric acid.

2.3 Corrosion analysis method

To investigate the SCC behavior of the alloy, the slow strain rate tensile (SSRT) tests were conducted separately in air and in 3.5 wt.% sodium chloride solution at a strain rate of $1\times10^{-6}\ s^{-1}$. The schematic diagram of the sample is depicted in Fig. 1. To quantify the SCC sensitivity of the four alloys, the ratio of ductility (D) and strength (S) was measured in 3.5 wt.% NaCl solution and in air, respectively. The measured values were then employed to evaluate the SCC sensitivity (P_{SCC}) according to the following formula [15]:

$$P_{SCC}\text{-Elongation}=\frac{D_{NaCl}}{D_{air}}\times100\% \quad (1)$$

$$P_{SCC}\text{-Strength}=\frac{S_{NaCl}}{S_{air}}\times100\% \quad (2)$$

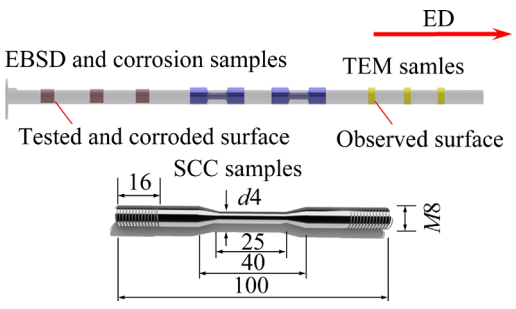

Fig. 1 Schematic diagram of sampling for corrosion testing and related characterization (unit: mm)

The intergranular corrosion (IGC) test was carried out according to the ASTM G110—92 standard [16]. The four alloys were immersed in an electrolyte consisting of 10 mL H_2O_2, 57 g NaCl, and 1000 mL distilled water at (35±1) °C for 6 h. The resultant corrosion depth was afterward measured using a LEICA DM−2500M optical microscope. The exfoliation corrosion (EXCO) was conducted as per the ASTM G34 standard [17] in a solution composed of 4.0 mol NaCl, 0.5 mol KNO_3, 0.1 mol HNO_3 and 1 L deionized water at 25°C for 48 h. The micro-morphology of the alloys after EXCO was observed by employing a KEYENCE VHX−7000 type 3D laser confocal microscope (LCM).

3 Results

3.1 Microstructure

The EBSD results for the four solid solution alloys are shown in Fig. 2. The 0-Ce alloy exhibited coarse grains and complete recrystallization, revealing the random texture orientation (Fig. 2(a)). In contrast, three Ce-containing alloys presented a substantial reduction in grain size, accompanied by the texture-orientation shift towards the {001} and {111} (Figs. 2(b−d)). The previous work has shown that the kernel average misorientation (KAM) between the nucleation site and its neighboring points is related to the local geometrically-necessary dislocation density [18]. Figures 2(e−h) display the KAM images for the four alloys generated from the CHANNEL 5 software. Compared to the 0-Ce alloy, the Ce-containing alloys displayed prominent green patches within the crystals, indicating an increase in intragranular dislocation density. As evidenced by the corresponding frequency distribution of KAM values, the low-degree KAM value (below 0.25°) of the 0-Ce alloy accounted for about 80%, with an average of about 0.20° (Fig. 2(i)). In contrast, the KAM distribution for the three Ce-containing alloys shifted toward the higher degrees, while the corresponding average KAM values increased to 0.89°−0.95° (Figs. 2(j−l)). This shift is attributed to the significant recrystallization inhibition induced by the Al−Ce intermetallic compounds, resulting in a high dislocation density within the alloys.

Figure 3 depicts the statistical data derived from the EBSD analysis, including the grain size, the fraction of deformed and recrystallized grains,

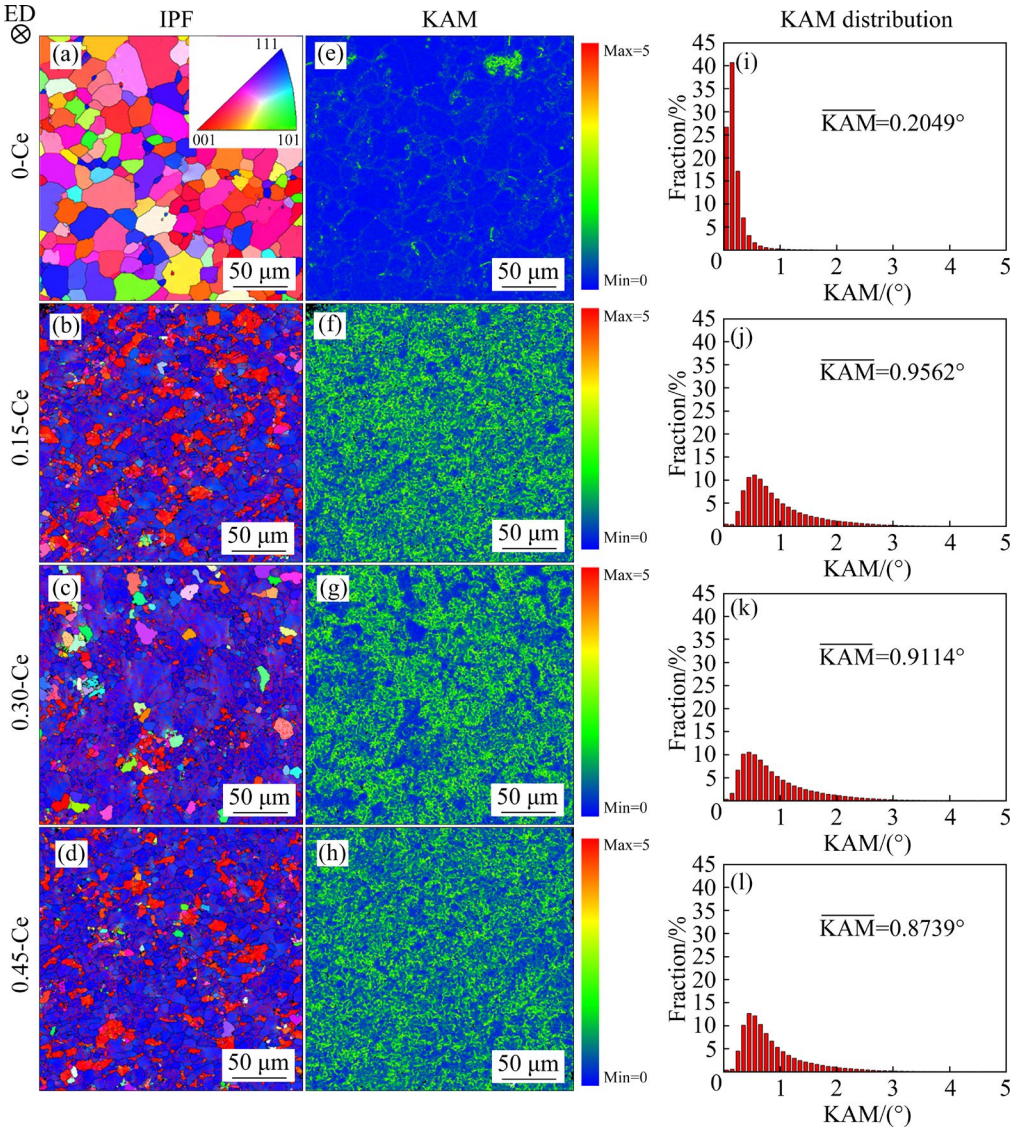

Fig. 2 EBSD images of solid solutions of four alloys with varying Ce contents: (a−d) IPF maps; (e−h) KAM images; (i−l) Frequency distributions and average KAM values

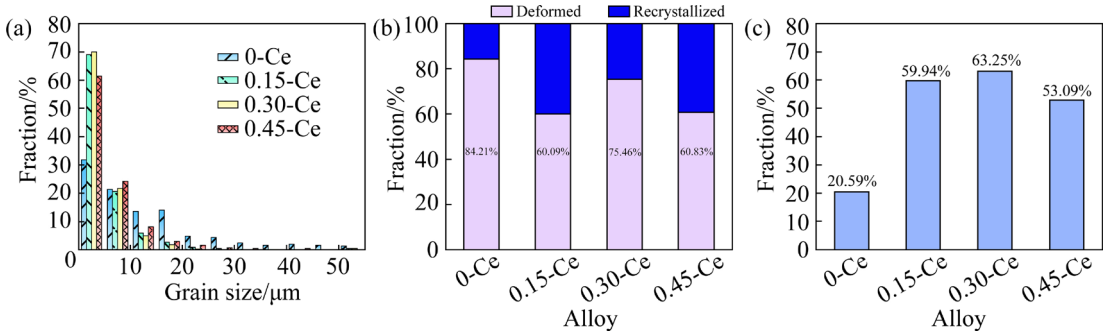

Fig. 3 EBSD results after statistical analysis of four alloys with varying Ce contents: (a) Grain size distributions; (b) Fractions of deformed recrystallized grains; (c) Proportions of LAGBs (misorientation angle <15°)

as well as the fraction of LAGBs in the alloy. With the addition of Ce, there was a noticeable rise in the percentage of small grains (less than 5 μm), while the percentage of large grains (greater than 10 μm) decreased correspondingly, as illustrated in Fig. 3(a). The average grain sizes for the 0-Ce, 0.15-Ce, 0.3-Ce, and 0.45-Ce alloys were 12.961, 4.675, 4.439, and 5.477 μm, respectively. The fraction of

deformed and recrystallized grains, determined based on the GOS value, is presented in Fig. 3(b). The 0-Ce alloy exhibited a recrystallization fraction of approximately 84.21%, remarkably higher than that of Ce-containing alloys. According to the percentages of LAGBs for each alloy in Fig. 3(c), the proportion of LAGBs in the 0-Ce alloy was only 20.59%, whereas Ce-containing alloys possessed LAGB fractions above 53%. The LAGB fraction initially increased and then decreased with the addition of Ce, correlating with the trend in grain refinement.

The microstructures of the alloys with the corresponding selected area electron diffraction (SAED) are shown in Fig. 4. In the 0-Ce alloy (Fig. 4(a)), there were numerous fine precipitates interspersed with several black particles. The EDS data acquired on the black particles (inset of Fig. 4(a)) revealed a substantial presence of Zr in addition to the matrix elements, confirming the

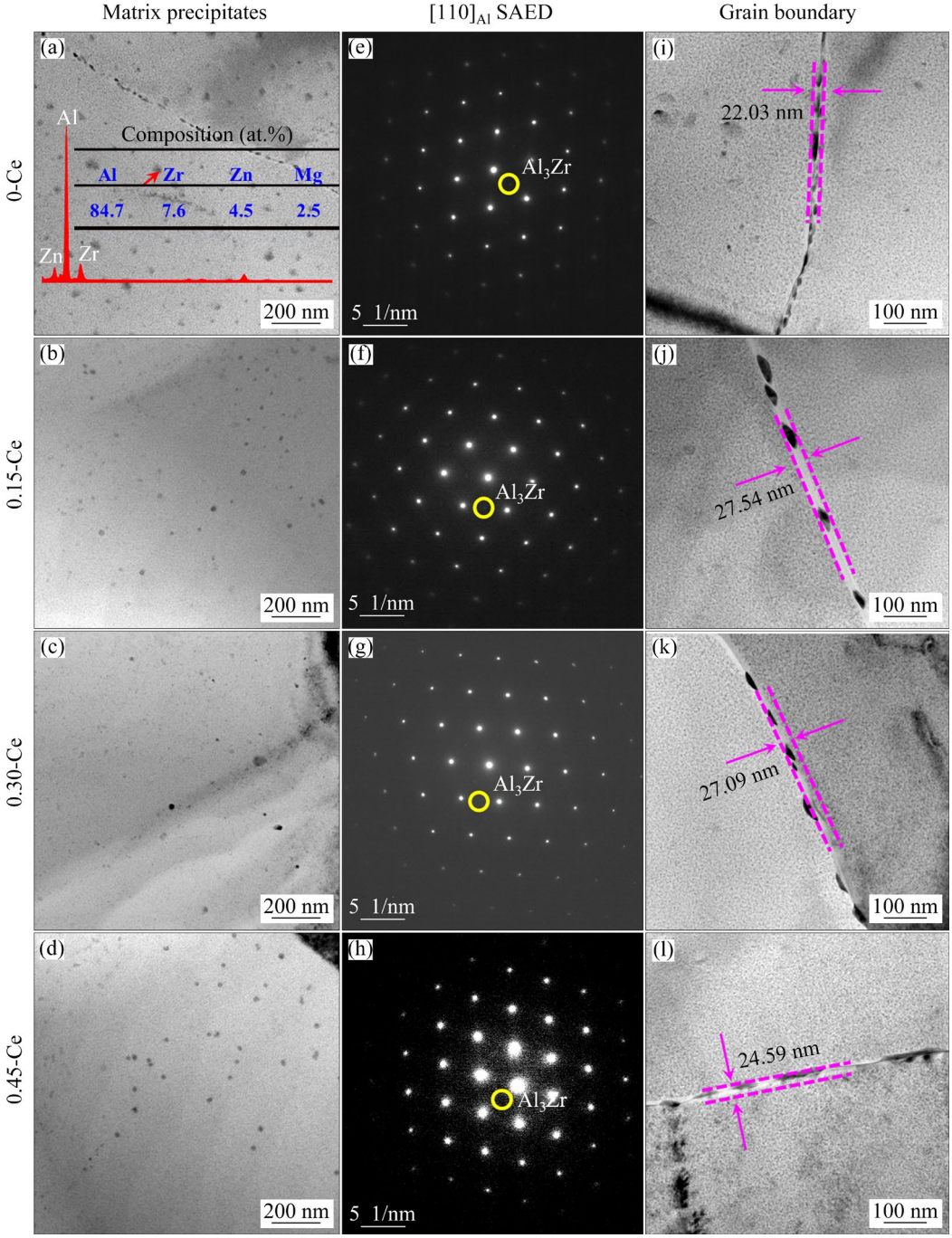

Fig. 4 TEM images along $[110]_{Al}$ zone axis (a−d), corresponding SAED patterns (e−h) and morphological images of grain boundary (i−l) in alloys with varying Ce contents

black particles as Al_3Zr. Figures 4(b–d) showed that the microstructures of the three Ce-alloys were rich in black Al_3Zr particles and remarkably similar to that of the 0-Ce alloy. Besides the diffraction of the Al matrix, the faint $\{110\}_{Al}$ diffraction spots related to the $L1_2$-Al_3Zr were discernible in the matching SAED patterns of the four alloys (Figs. 4(e–h)). It could be seen that the addition of Ce exerted a minimal effect on the $L1_2$-Al_3Zr. As for the microstructures of grain boundaries in the four alloys, the small and dense grain boundary precipitates (GBPs) in the 0-Ce alloy were continuously distributed, displaying a precipitate-free zone (PFZ) width of approximately 22.03 nm (Fig. 4(i)). In the three Ce-containing alloys, coarse GBPs were intermittently arranged along the grain boundaries, while the PFZs exhibited slight broadening (Figs. 4(j–l)).

Figure 5 displays the Ce-containing IMCs in the 0.45-Ce alloy. An elliptical particle of roughly 0.4 μm was observed at the grain boundaries of the alloy (Fig. 5(a)). The subsequent mapping revealed that the particle primarily consisted of Al, Zn, and Cu along with a small amount of Ce (Figs. 5(b–g)). By correlating its SAED (Fig. 5(b)) and elemental color distribution images, this particle was identified as $Al_{13}(Zn,Cu)_{13}Ce_2$.

In the 0.45-Ce alloy, several small spherical particles were also detected, and one of them was further characterized in Fig. 6. From Fig. 6(a), it could be seen that the size of the spherical particles was approximately 100 nm. The corresponding HRTEM image showed a smooth interface between the particle and the Al matrix, proving that there was no orientation relationship (Fig. 6(b)). The subsequent EDS analysis demonstrated that the spherical particle contained high contents of Al, Zn, Cu, and Ce, and trace Mg (Fig. 6(c)). The combination of SAED patterns with elemental distribution results enabled the nano-spherical particles to be identified as $(Zn,Al,Cu)_{22}Ce_3$ (Figs. 6(d–h)).

Figure 7 displays $\langle 110\rangle_{Al}$-orientated HRTEM images of the four alloys. In Fig. 7(a), some spherical precipitates measuring approximately 2−3 nm could be observed, which exhibited good coherence with the Al matrix, hence referred to as the GP I zone. The corresponding Fast Fourier Transform (FFT) (inset in Fig. 7(a)) showed a weak diffraction at the 1/3 and 2/3 $\{220\}_{Al}$, being indicative of the η' phase [19]. The weak 1/3 and 2/3 $\{220\}_{Al}$ diffraction also suggested the presence of scarce η' phase in the 0-Ce alloy. The three Ce-containing alloys possessed analogous microstructures, in which the coarse precipitates interspersed among numerous GP I zones, maintaining a semi-coherent relationship with the Al matrix (Figs. 7(b–d)). The FFT images inserted in Figs. 7(b–d) revealed the prominent η'-related diffraction spots, indicating a significant increase in the quantity of the η' phase in the three Ce-containing alloys.

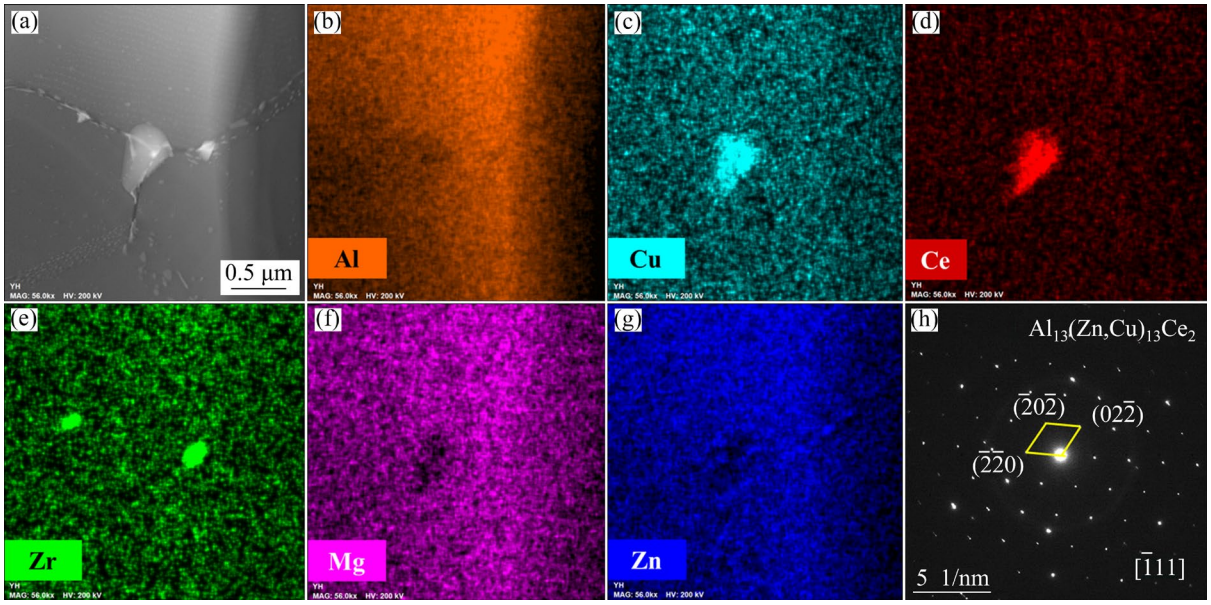

Fig. 5 Bright-field TEM images of IMC located at grain boundary (a), corresponding element scan (b–g) and SAED patterns of IMC (h) in 0.45-Ce alloy

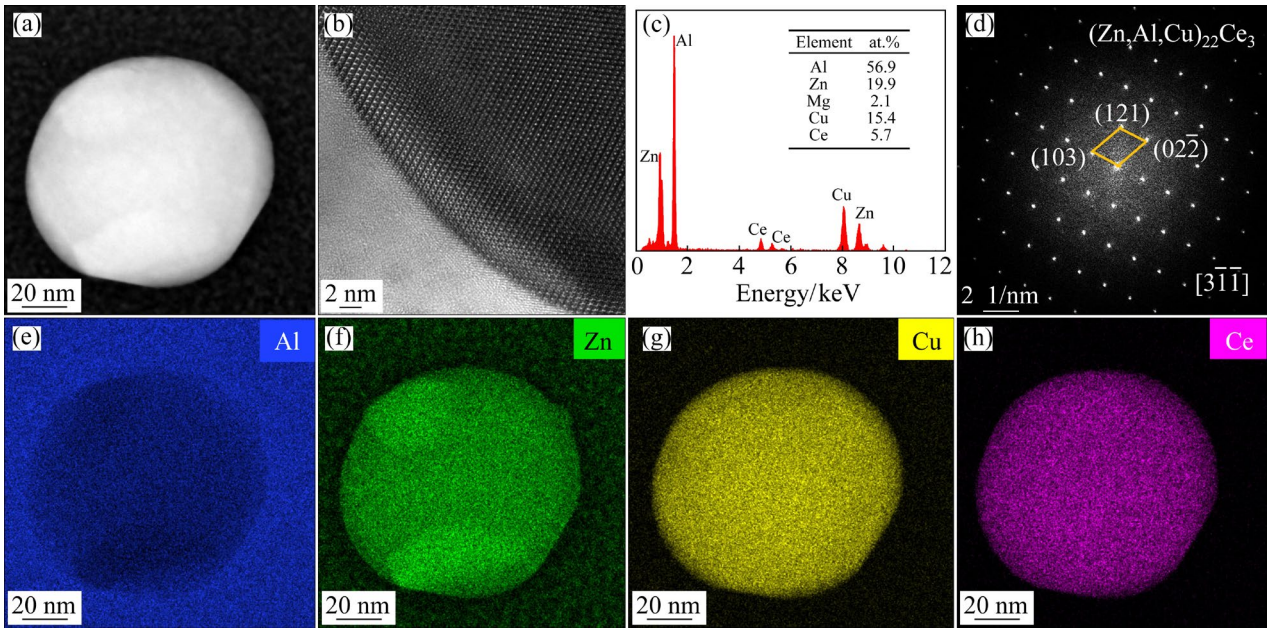

Fig. 6 TEM image of nano-spherical particle in 0.45-Ce alloy (a); HRTEM image of spherical particle (b); EDS results of spherical particle (c); SAED patterns of spherical particle (d); Corresponding element scans (e−h)

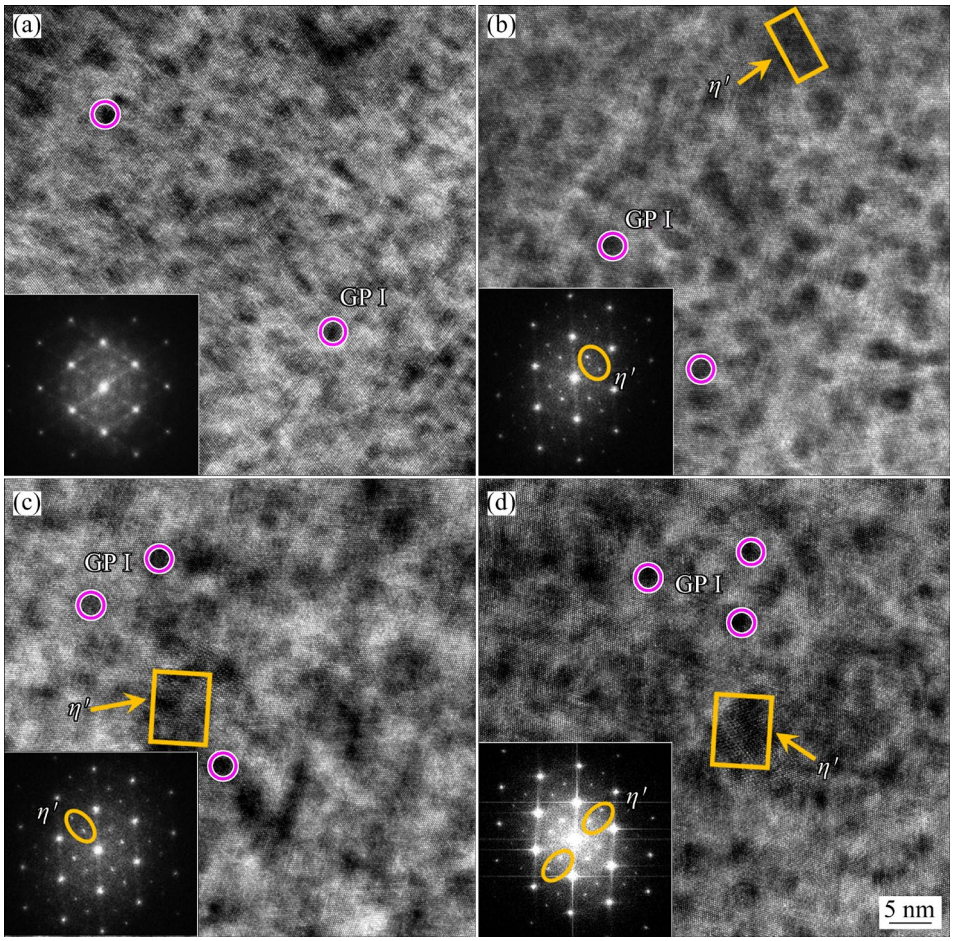

Fig. 7 $\langle 110 \rangle_{Al}$ orientation HRTEM images and corresponding FFT patterns of four alloys with varying Ce contents: (a) 0-Ce; (b) 0.15-Ce; (c) 0.3-Ce; (d) 0.45-Ce

3.2 SCC analysis

Figure 8 depicts the SSRT curves obtained in air and in 3.5 wt.% NaCl solution, and the results are given in Table 2. The P_{SCC} values corresponding to the strength and ductility of the four alloys are listed in Table 2. Under the above conditions, the mechanical properties and strength ratio of the three Ce-containing alloys surpassed those of the 0-Ce alloy, indicating that the addition of Ce effectively improved the resistance to SCC. With the increase in the Ce content, the P_{SCC} of strength gradually decreased. Notably, the best combination of strength and elongation was achieved in the 0.15-Ce alloy in the 3.5 wt.% NaCl solution.

Figure 9 displays the fracture surfaces of four alloys after the SSRT testing in 3.5 wt.% NaCl solution, and the relevant EDS data are summarized in Table 3. The fracture morphology of the 0-Ce alloy, depicted in Fig. 9(a), was mainly composed of "sugar-like" grains with noticeable coarse cracks at the grain edges (red arrows). Additionally, numerous small white particles were observed on the fracture surfaces. The mapping and EDS results revealed that most of the fracture surface was covered by corrosion products (Figs. 9(b−d)). The high content of O indicated the cathodic reduction of O_2 to generate OH^-, thus forming the main corrosion product of $Al(OH)_3$ [20]. Compared with the 0-Ce alloy, the fracture surface of the 0.15-Ce alloy possessed multiple deep and coarse dimples (about 5 μm in size), indicating a typical ductile fracture (Fig. 9(e)). The EDS results showed that the central region (Spectrum B) of dimple on the fracture surface had Al, O, and Ce elements. The mapping in Figs. 9(f−h) displayed the substantial presence of $Al(OH)_3$ on the local grains alongside uniformly distributed Ce-oxides. The fracture surface of the 0.3-Ce alloy was similar to that of the 0.15-Ce alloy, exhibiting the distribution of Ce-oxides, but the number of dimples was reduced (Figs. 9(i, j)). The BSE image in Fig. 9(k) revealed numerous micro-cracks (red arrows) primarily originating from the bright IMCs. The EDS analysis in Fig. 9(k) indicated that these bright IMCs contained significant amounts of Al, Zn, Cu, and trace amounts of Ce and O. Following SSRT testing in 3.5 wt.% NaCl solution, the fracture surface of the 0.45-Ce alloy exhibited numberous cracks within

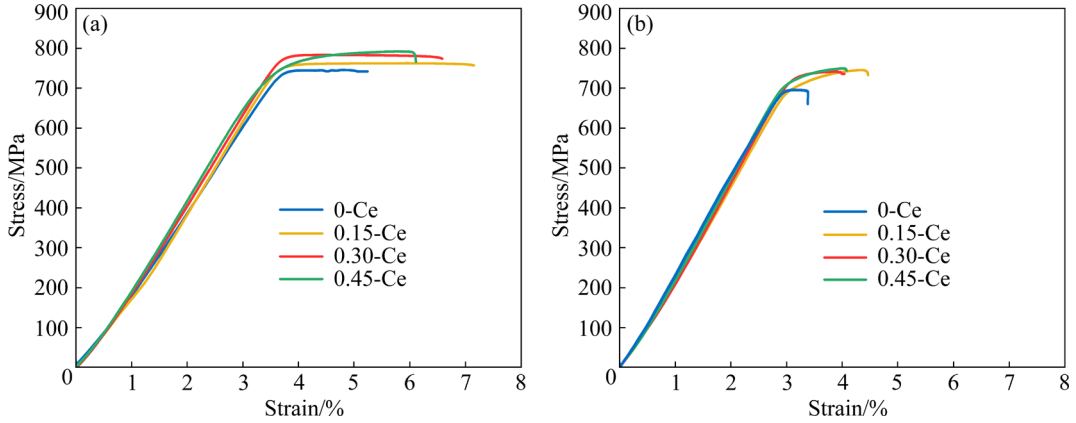

Fig. 8 SSRT curves of four alloys with varying Ce contents: (a) In air; (b) In 3.5 wt.% NaCl solution

Table 2 SSRT results and calculated P_{SCC} values of samples

Sample	Environment	UTS/MPa	YS/MPa	Elongation/%	P_{SCC}-UTS/%	P_{SCC}-YS/%	P_{SCC}-Elongation/%
0-Ce	Air	745.4	724.4	5.2	93.2	94.0	63.5
	3.5 wt.% NaCl	695.1	681.0	3.3			
0.15-Ce	Air	762.3	738.1	7.1	97.7	95.5	64.8
	3.5 wt.% NaCl	744.8	704.8	4.6			
0.30-Ce	Air	783.4	749.5	6.5	94.5	98.1	63.1
	3.5 wt.% NaCl	740.7	735.2	4.1			
0.45-Ce	Air	792.1	737.8	6.1	94.5	98.0	67.2
	3.5 wt.% NaCl	748.9	723.4	4.1			

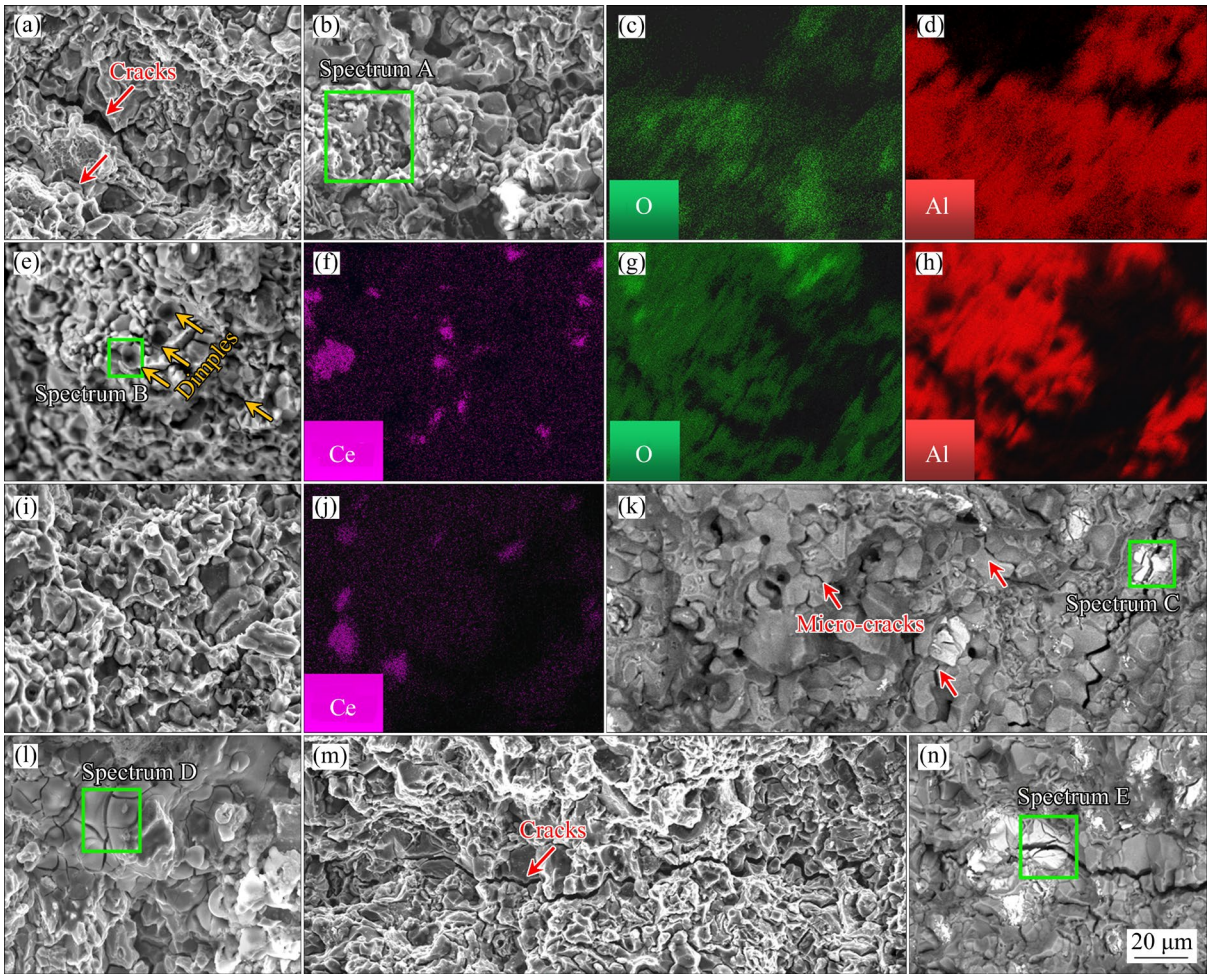

Fig. 9 SEM images of typical fracture surfaces of four alloys with varying Ce contents after SSRT in 3.5 wt.% NaCl solution: (a, b) Low-magnified images of 0-Ce alloy; (c, d) Element surface scans in (b); (e) Low-magnified image of 0.15-Ce alloy; (f−h) Element surface scans in (e); (i) Low-magnified image of 0.3 Ce-alloy; (j) Ce element scan in (i); (k) BSE image in (i); (l, m) Low-magnified images of 0.45-Ce alloy; (n) BSE image of crack source in (l)

Table 3 EDS results from various points in Fig. 9 (at.%)

Spectrum	Al	Zn	Mg	Cu	Ce	Cl	Na	O
A	40.69	1.80	1.57	0.62	–	2.02	0.01	53.30
B	32.01	27.65	2.23	3.57	3.81	–	–	30.73
C	21.08	44.03	0.70	24.07	5.12	–	–	5.00
D	31.68	0.97	1.12	0.26	–	2.51	–	63.39
E	35.94	40.50	4.24	14.15	1.28	–	–	3.89

the corrosion products that were detected to be $Al(OH)_3$ by EDS (Fig. 9(k)). Additionally, there were coarse cracks across the entire fracture surface, which also originated from the white Al−Zn−Cu−Ce compounds (Figs. 9(l, m)). Under the combined action of corrosive media and tensile stress, these coarse IMCs acted as the sources of cracks.

3.3 IGC analysis

The IGC cross-sections of specimens with different Ce contents are depicted in Fig. 10. In the 0-Ce alloy, a corrosion trace of approximately 200 μm was observed (Fig. 10(a). In comparison to the 0-Ce alloy, the corrosion depths of all Ce-containing alloys decreased below 100 μm (Figs. 10(b−d)). Increasing the Ce content from 0.15

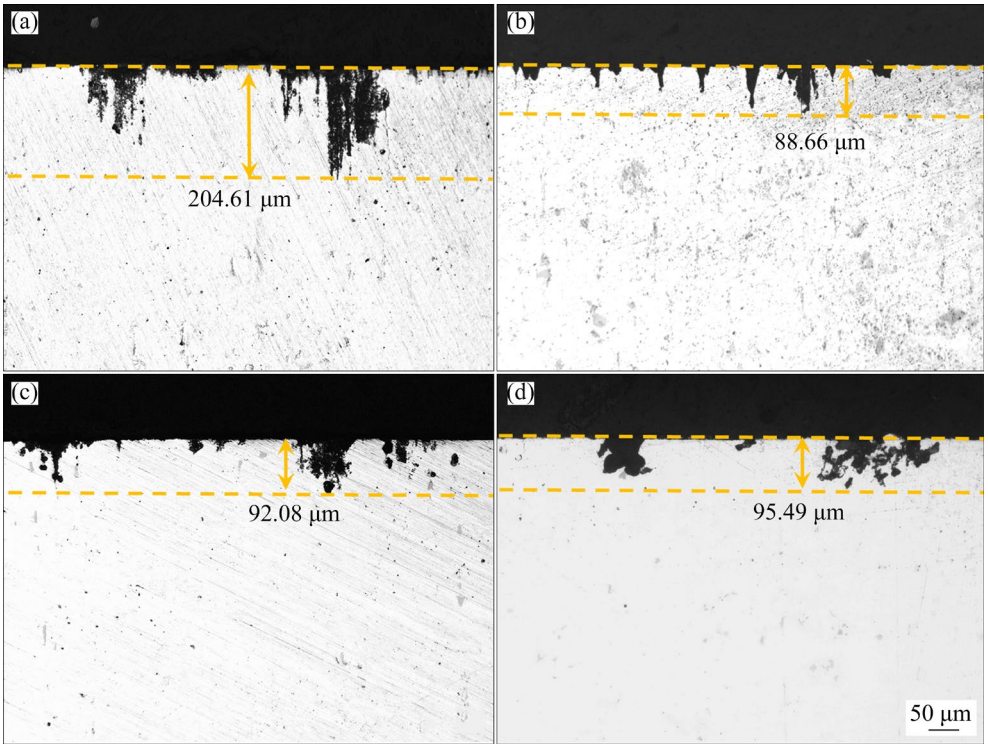

Fig. 10 IGC morphology of alloys with varying Ce contents: (a) 0-Ce; (b) 0.15-Ce; (c) 0.3-Ce; (d) 0.45-Ce

to 0.45 wt.% resulted in a rise in the maximum IGC depth from 88 to 95 μm, indicating a slight increase in the sensitivity of IGC.

3.4 EXCO analysis

The surface of the alloy after the EXCO test was characterized by 3D-LCM, as shown in Fig. 11. The unevenness of the surface after immersion in the etching solution reflected the different degrees of corrosion within the alloy. The surface of the 0-Ce alloy exhibited numerous deep pits and corrosion products (Fig. 11(a)). The distance between the deepest and highest points of the corroded surface was approximately 103 μm, resulting in a surface roughness (R_a) of 11.29 μm (Figs. 11(a, b)). After corrosion, the 0.15-Ce and 0.3-Ce alloys exhibited flatter surfaces with abundant cavities. As seen from Figs. 11(c−f), the differences in depth were reduced to 44−54 μm, and the respective R_a values decreased to around 4 μm. With further increase of Ce content to 0.45 wt.%, the corroded alloy surface became rougher, and the R_a value increased to 7.34 μm (Figs. 11(g, h)). This indicated that the reasonable addition of Ce effectively reduced the exfoliation corrosion depth of the alloy, thus enhancing its resistance to severe corrosion.

4 Discussion

4.1 Effect of Ce on microstructure of alloy

The rare earth elements in aluminum alloys typically exist in three forms: solid solutions, segregations at grain boundaries, and compounds [7]. According to the Hume−Rothery rule [21], compounds are easier to form when there is a significant difference in electronegativity between alloying elements. The electronegativity difference between Ce (1.12) and Al (1.61), Zn (1.65), or Cu (1.90) is greater than that between Ce (1.12) and Mg (1.31). Consequently, Ce in the Al−Zn−Mg−Cu alloy has a higher tendency to bond with Al, Zn, and Cu to form secondary phase particles (nano-spherical $(Zn,Al,Cu)_{22}Ce_3$ in Fig. 6). During alloy solidification, these secondary phase particles suppress grain growth by reducing driving force or inhibiting grain boundary migration. The nanoscale $(Zn,Al,Cu)_{22}Ce_3$ and $L1_2$-Al_3Zr particles effectively pin dislocations and inhibit their movement, thereby stabilizing the deformed substructure and suppressing the recrystallization nucleation [11].

When the concentration of Ce surpasses the maximum solubility limit, multiple Ce atoms can combine with other elements in the alloy to form

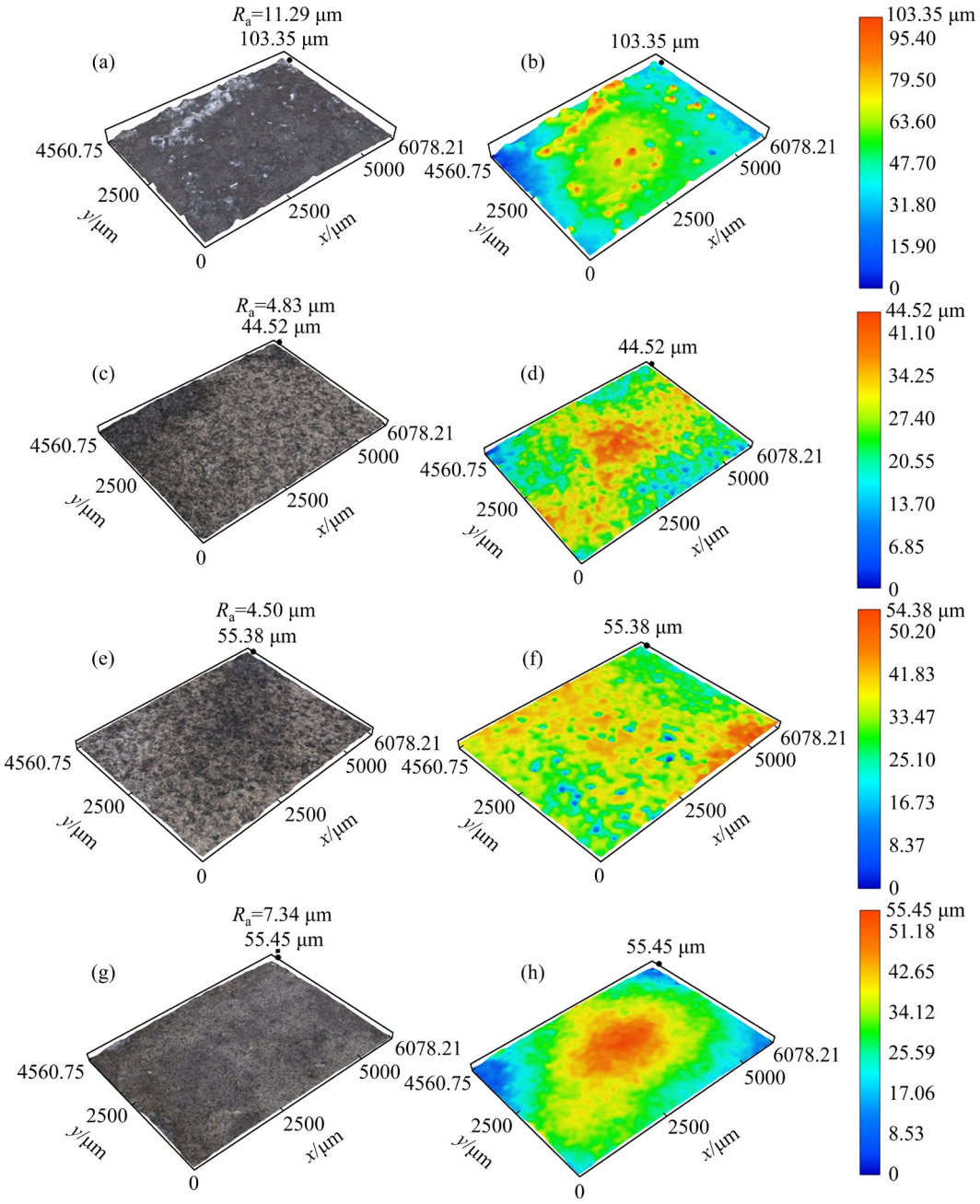

Fig. 11 Micro-morphologies (a, c, e, g) and 3D surface topographies (b, d, f, h) after EXCO of alloys with varying Ce contents: (a, b) 0-Ce; (c, d) 0.15-Ce; (e, f) 0.3-Ce; (g, h) 0.45-Ce

coarse compounds. Therefore, excess Ce atoms were found in the $Al_{13}(Zn,Cu)_{13}Ce_2$ phase, which also accounted for the absence of Mg in the Ce-containing IMCs (Fig. 5).

4.2 Effect of Ce on precipitates and grain boundary characteristics

The effect of Ce on the aging precipitation process of the Al alloy has been proven in many studies [22−24]. WANG et al [23] and LAI et al [24] have elucidated the main factors that delay the development of the GP zone and accelerate the precipitation of the η' phase in Ce-containing alloys. The Ce atoms possess a high vacancy binding energy [24,25]. Hence, when Ce is added to the Al matrix, some Ce atoms occupy vacancies, hindering the nucleation of the GP zone. Since Ce atomic size (0.27 nm) exceeds that of Al (0.182 nm), the lattice distortion of the Al matrix and the increase in the energy of the system occur. To maintain the energy balance of the system, Ce atoms gather numerous vacancies around them, forming Ce-vacancy

clusters [24]. These clusters act as nucleation sites for the precipitate phase and facilitate the diffusion of solid-solution atoms (Zn, Mg, and Cu) into them, thereby accelerating the phase transition from GP zones to the η' phase.

The Ce atom with higher vacancy binding energy also interferes with the nucleation of GBPs. Likewise, Ce atoms occupy some vacancies at the grain boundaries, attracting the surrounding vacancies and forming Ce-vacancy clusters which afterward serve as nucleation sites for GBPs. However, the scarcity of vacancies in other regions hinders precipitation, causing a buildup of solute atoms at Ce-vacancy clusters within a short period, ultimately resulting in the coarsening of GBPs. In Ce-containing alloys, the number of GBPs at the equivalent grain boundary lengths decreased compared to 0-Ce alloys, indicating a discontinuous distribution of GBPs. Furthermore, both GBPs and PFZs in Ce-containing alloys became thicker and wider, respectively. With further increase in the Ce content, vacancies near the grain boundaries were further occupied and absorbed, leading to a decrease in the diffusion of solid solution atoms toward the grain boundaries and the narrowing of PFZs.

4.3 Effect of Ce on mechanical properties

According to the Hall−Petch equation, the equation for grain boundary strengthening $\Delta\sigma_{gb}$ is [26]

$$\Delta\sigma_{gb}=kd^{-1/2} \tag{3}$$

where d represents the grain diameter obtained from EBSD data, and k is a constant (0.12 MPa·m$^{-1/2}$ for A7075 alloy). The EBSD results revealed that the average grain sizes of the alloy with Ce contents ranging from 0 to 0.45 wt.% were 12.961, 4.675, 4.439, and 5.477 μm, respectively, and the corresponding grain boundary strengthening values were 33.3, 55.5, 56.9, and 51.3 MPa. In comparison to the 0-Ce alloy, the grain boundary strengthening of the three Ce-containing alloys increased by approximately 20 MPa.

As aforementioned in Section 4.2, Ce atoms play a significant role in the precipitation of the alloy by interacting with crystal defects. The statistical analysis was conducted on at least 200 precipitates from the HRTEM images obtained from each alloy, and the average radius of the precipitate phase was evaluated, as illustrated in Fig. S1 (in Supplementary Materials). It was observed that with the increase in Ce content, the average radius of precipitates gradually increased. Under identical aging durations, the aging of three Ce-containing alloys was accelerated, accompanied by the increase in the proportion of η' precipitates. This trend became more pronounced with increasing Ce content. The increase of η' precipitates was an important factor contributing to the gradual enhancement of the tensile strength of the alloy (Fig. 8 and Table 2). Furthermore, Ce can also absorb hydrogen, nitrogen, and other gases in the as-cast structure, causing the disappearance of defects including holes and cracks [27]. This is also another crucial factor contributing to the improved mechanical properties of Ce-containing alloys. However, the presence of coarse Al−Zn−Cu−Ce intermetallic compounds in alloys with high Ce content was inevitably detrimental to the ductility of the alloy.

4.4 Effect of Ce on corrosion resistance

The outcomes of all the corrosion tests highlighted that the 0-Ce alloy exhibited the higher corrosion sensitivity and the poorer corrosion resistance. The corrosion resistance of three Ce-containing alloys was improved by the following microstructural modifications: (1) altering the grain boundary characteristics; (2) inhibiting the recrystallization and grain refinement as well as the existence of numerous dislocations; (3) forming Ce-rich phases.

4.4.1 Effect of grain boundary characteristics on corrosion resistance

As a region where precipitates, defects, and impurities tend to segregate, the grain boundary shows higher activity compared to the interior of grains. Hence, the grain boundary characteristics substantially affect the sensitivity of the alloy to IGC, EXCO, and SCC. These corrosion mechanisms are primarily influenced by a combination of anodic dissolution and hydrogen embrittlement (HE) [28,29].

The corrosion potentials (φ_{corr}) for PFZ, η' phase at grain boundaries, and Al matrix of the aged 7A04 alloy were reported to be −0.57, −0.86, and −0.68 V, respectively [30]. The difference in φ_{cor} values between the η' phase and the Al matrix surpasses that between PFZ and the Al matrix. This

indicates that the corrosion potential of the η' phase is more anodic compared to both the Al matrix and PFZ, leading to its preferential dissolution followed by the formation of hydrogen and corrosion pits. The reactions are as follows [31]:

$$Al^{3+}+H_2O=AlOH^{2+}+H^+ \quad (4)$$

$$Al^{3+}+2H_2O=Al(OH)_2^++2H^+ \quad (5)$$

$$Al^{3+}+3H_2O=Al(OH)_3+3H^+ \quad (6)$$

As a product of the dissolution reaction, the $Al(OH)_3$ accumulates on the surface of the alloy (Fig. 9). Some H atoms combine to form H_2, while the remaining hydrogen infiltrates the Al lattice along dislocations and grain boundaries, resulting in lattice embrittlement and intergranular fracture. In the initial stage of SCC, the pre-existing oxide film on the alloy surface gradually breaks down under tension. Subsequently, Cl^- infiltrates the ruptured oxide film, resulting in the generation of Al^{3+}, Cl^-, and H^+ ions on the exposed surface. The continuity of GBPs in the 0-Ce alloy accelerated the dissolution of grain boundaries, facilitating crack formation and propagation under the SSRT. Additionally, the narrow PFZ in the 0-Ce alloy easily extends corrosion paths into the grains, accelerating the occurrence of HE and further diminishing the SCC resistance [30]. The presence of numerous cracks on the fracture surface of SCC in the 0-Ce alloy indicated that grain boundaries were the preferred paths for crack propagation.

The SCC mechanism for Ce-containing alloys is summarized in Fig. 12(b). The addition of Ce causes the intermittent distribution of coarse GBPs, which hinders anodic dissolution along the grain boundaries. This further reduces the generation of atomic H and inhibits the occurrence of HE. The coarse and discontinuous GBPs serve as the H trapping sites, diminishing the H concentration, alleviating the stress concentration at the crack source, and effectively inhibiting the propagation of corrosion cracks [32]. The decrease in the amount of coarse cracks in Ce-containing alloys after the exposure to 3.5 wt.% NaCl solution under the SSRT confirmed this point. Furthermore, the appropriate broadening of the PFZ in the Ce-containing alloys further alleviated the expansion of corrosion-induced cracks, obstructing the diffusion of the corrosive solution into the interior of grains, which also increased the SCC resistance of the alloys.

4.4.2 Effect of grain refinement and crystal defects on corrosion resistance

As per the EBSD findings, Ce addition refined the grain size, significantly increased the density of crystal defects (subgrain boundaries, dislocations, etc), and suppressed the recrystallization. Because of the lower energy of LAGBs and sparse precipitates, the generation of GBPs is more inclined to form along HAGBs, thereby leading to the initiation and development of corrosion along them [15,33]. The high density of dislocations and subgrain boundaries can also provide more stored energy for the rapid formation and growth of passive films [34,35], accelerating the repair process of oxide films. In Ce-containing alloys, the grain refinement significantly increases the

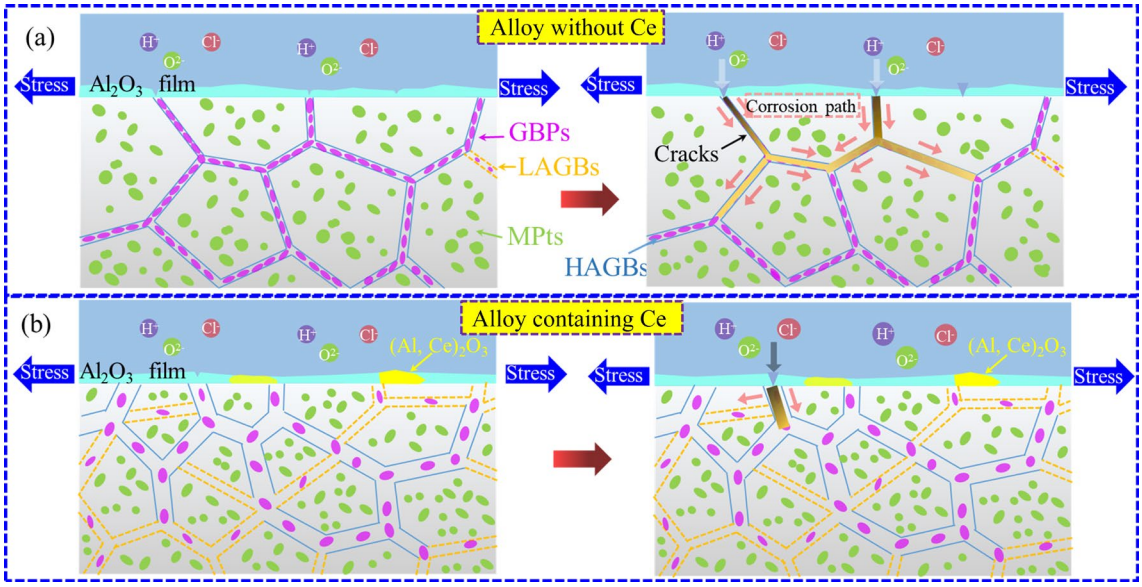

Fig. 12 Schematic diagram showing mechanism of SCC on 0-Ce (a) and Ce-containing (b) alloys

proportion of grain boundaries, and more grain boundaries can carry more external loads, thus reducing the possibility of cracking at grain boundaries [36,37]. Similar results were reported by ARGADE et al [38], where grain refinement also facilitated the formation of dense and stable passive films. Additionally, TSAI and CHUANG [39] found that the significant reduction in grain size induced a wave-like dislocation slip pattern in the alloy, leading to the uniform distribution of strain, which significantly improved the SCC resistance of the 7475 alloy.

4.4.3 Effect of Ce-rich phases on corrosion

When the Ce-containing alloy is exposed to the corrosive medium, Ce and Al atoms can simultaneously oxidize to produce a composite oxide film (Al_2O_3 and Ce_2O_3, and $(Al,Ce)_2O_3$) [11]. MICHALIKA et al [40] also believed that in an environment containing chloride ions, the Ce within the alloy may form a passive film primarily composed of $Ce(OH)_3$ and Ce_2O_3. This phenomenon was also confirmed in Fig. 9.

Since the electrode potential of the Ce atom is more negative than that of the Al atom, electrons generated by Ce—O bonds will be transferred to the Al—O bonds. This process increases the electron cloud density, thereby enhancing the bonding force of the Al—O bonds [11]. The enhanced consolidation and stabilization of the passive film effectively suppress the extensive dissolution of the alloy. Additionally, the extensive coverage of the passive film reduces the available surface area for corrosion, subsequently reducing the corrosion rate. However, with the increase in Ce content, the size and quantity of coarse Ce-containing IMCs in the alloy gradually increase. These coarse IMCs become the sites for the source of SCC (Fig. 9), increasing the depth and the range of corrosion damage to the alloy. Consequently, excessive Ce addition can degrade both the corrosion resistance and toughness of the alloy.

5 Conclusions

(1) The addition of Ce formed $(Zn,Al,Cu)_{22}Ce_3$ phases with dimensions of 100 nm in the alloy. These $(Zn,Al,Cu)_{22}Ce_3$ suppressed the recrystallization of the alloy, which significantly increased the dislocation density and the proportion of LAGBs, leading to grain refinement. The Ce-vacancy cluster facilitated the phase transition of GP zones to the η' phase, enabling the discontinuous distribution of coarse GBPs and the appropriate broadening of the PFZ.

(2) The introduction of Ce into the alloys resulted in a significant modification of the grain boundary, notably decreasing the likelihood of HE and impeding the formation and spread of cracks. By suppressing recrystallization and enhancing internal crystal defects, the alloy effectively restricted the expansion of HE and accelerated the formation and repair capability of the passive film. The presence of Ce-rich phases within the alloy further enhanced the stability of the passive film and impeded its dissolution. The modifications induced by the addition of Ce notably enhanced the overall corrosion resistance of the investigated alloy.

(3) With the increase in Ce content in the alloy from 0.15 to 0.45 wt.%, an excess of Ce atoms formed the bulk IMCs, consequently diminishing the corrosion resistance of the alloy. The alloy containing 0.15 wt.% Ce achieved the best corrosion resistance.

CRediT authorship contribution statement

Chen LI: Conceptualization, Methodology, Validation, Writing − Original draft, Writing − Review & editing, Formal analysis; **Yun-tian LUO:** Conceptualization, Resources, Formal analysis, Writing − Review & editing; **Qing-shan ZHOU:** Validation, Investigation, Resources, Writing − Review & editing; **Meng-nan HAN:** Resources, Formal analysis, Writing − Review & editing; **Shao-hui SHA:** Resources, Formal analysis, Writing − Review & editing; **Xiao-jing XU:** Supervision, Conceptualization, Formal analysis, Writing − Review & editing, Validation.

Declaration of competing interest

The authors declare that they have no known competing financial interests or personal relationships that could have appeared to influence the work reported in this paper.

Acknowledgments

This work was financially supported from the Key Project of Equipment Pre-research Foundation of the Ministry of Equipment Development of the Central Military Commission of China (No. 6140922010201), and the Key Project of Research and Development of Zhenjiang Province, China (No. GY2018021).

Supplementary Materials

Supplementary Materials in this paper can be found at: http://tnmsc.csu.edu.cn/download/03-p2148-2023-1339-Supplementary_Materials.pdf.

References

[1] ZHANG Meng-han, LIU Sheng-dan, JIANG Jing-yu, WEI Wei-chang. Effect of Cu content on intergranular corrosion and exfoliation corrosion susceptibility of Al−Zn−Mg−(Cu) alloys [J]. Transactions of Nonferrous Metals Society of China, 2023, 33: 1963−1976.

[2] JUAN Yong-fei, NIU Guo-shuai, YANG Yang, XU Zi-han, YANG Jian, TANG Wen-qi, JIANG Hai-tao, HAN Yan-feng, DAI Yong-bing, ZHANG Jiao, SUN Bao-de. Accelerated design of Al−Zn−Mg−Cu alloys via machine learning [J]. Transactions of Nonferrous Metals Society of China, 2024, 34: 709−723.

[3] XU Xiao-jing, MAO Qiang, JIANG Ze, VITUS Table, ZHANG Tian-ci, JIA Wei-jie, ZHU Cheng-yu, WANG Hao. Effect of multi-stage solution and aging process on microstructure and properties of Al−11.2Zn−3.0Mg−1.3Cu−0.2Zr aluminum alloy extrusion [J]. Materials Letters, 2019, 254: 375−378.

[4] CAI Cheng-bin, XU Xiao-jing, HUANG Jin-dong, JU Shi-hao, DING Qing, WANG Cheng-song. Effect of pre-recovery on microstructure and properties of rolled Al−12.18Zn−3.31Mg−1.43Cu−0.20Zr−0.04Sr aluminum alloy [J]. International Journal of Minerals Metallurgy and Materials, 2019, 26(2): 241−250.

[5] TSAI Y C, CHOU C Y, LEE S L, LIN C K, LIN J C, LIM S W. Effect of trace La addition on the microstructures and mechanical properties of A356 (Al−7Si−0.35Mg) aluminum alloys [J]. Journal of Alloys and Compounds, 2009, 487: 157−162.

[6] WANG Yi-chang, WU Xiao-dong, YUE Lu, GUO Ming-xing, CAO Ling-fei. Aging precipitation behavior and properties of Al−Zn−Mg−Cu−Zr−Er alloy at different quenching rates [J]. Transactions of Nonferrous Metals Society of China, 2022, 32: 1070−1082.

[7] LI Chen, ZHOU Qing-shan, HAN Meng-nan, SHA Shao-hui, LUO Yun-tian, XU Xiao-jing. Effect of rare earth element Er on the microstructure and properties of highly alloyed Al−Zn−Mg−Cu−Zr−Ti alloy [J]. Journal of Alloys and Compounds, 2023, 956: 170248.

[8] LIN Gao-yong, LI Kun, FENG Di, FENG Yong-ping, SONG Wei-yuan, XIAO Meng-qiong. Effects of La−Ce addition on microstructure and mechanical properties of Al−18Si−4Cu−0.5Mg alloy [J]. Transactions of Nonferrous Metals Society of China, 2019, 29: 1592−1600.

[9] JIANG Jing-yu, JIANG Feng, ZHANG Meng-han. Microstructure evolution and mechanical properties of Al−Mg−Sc−Zr alloy sheet after friction stir welding [J]. Transactions of Nonferrous Metals Society of China, 2023, 33: 1687−1700.

[10] ZHOU Hai-tao, ZENG Xiao-qin, LIU Liu-fa, ZHANG Ya, ZHU Yan-ping, DING Wen-jiang. Effect of cerium on microstructures and mechanical properties of AZ61 wrought magnesium alloy [J]. Journal of Materials Science, 2004, 39: 7061−7066.

[11] HU Gui-yun, ZHU Chang-jun, XU Dao-fen, DONG Pegn-xuan, CHEN Kang-hua. Effect of cerium on microstructure, mechanical properties and corrosion properties of Al−Zn−Mg alloy [J]. Journal of Rare Earths, 2021, 39: 208−216.

[12] YANG Zi-wei, CHEN Chao, LI Dan, WU Yi-you, GENG Zhao-wen, KONAKOV V, ZHOU Ke-chao. An additively manufactured heat-resistant Al−Ce−Sc−Zr alloy: Microstructure, mechanical properties and thermal stability [J]. Materials Science and Engineering A, 2023, 872: 144965.

[13] LIU Y, MICHI R A, DUNAND D C. Cast near-eutectic Al−12.5wt.%Ce alloy with high coarsening and creep resistance [J]. Materials Science and Engineering A, 2019, 767: 138440.

[14] WANG Yi-chang, WU Xiao-dong, CAO Ling-fei, TONG Xin, COUPER M J, LIU Qing. Effect of trace Er on the microstructure and properties of Al−Zn−Mg−Cu−Zr alloys during heat treatments [J]. Materials Science and Engineering A, 2020, 792: 139807.

[15] PAN Yu-zhe, DUAN Shu-wei, GUO Fu-qiang, MATSUDA K J, WANG Tao, ZOU Yong. Stress corrosion inhibition mechanism of hot rolled medium thickness Al−Zn−Mg−Cu plate by cryogenic-aging treatment [J]. Journal of Materials Research and Technology, 2023, 23: 894−910.

[16] ASTM G110 — 92. Standard practice for evaluating intergranular corrosion resistance of heat treatable aluminum alloys by immersion in sodium chloride + hydrogen peroxide solution [S]. 1992.

[17] ASTM G34 — 01. Standard test method for exfoliation corrosion susceptibility in 2XXX and 7XXX series aluminum alloys (EXCO Test) [S]. 2001.

[18] LI Yong, WANG Yin, LU Bing, YU Wei, WANG Hai-yao, XU Guang-ming, WANG Zhao-dong. Effect of Cu content and Zn/Mg ratio on microstructure and mechanical properties of Al−Zn−Mg−Cu alloys [J]. Journal of Materials Research and Technology, 2022, 19: 3451−3460.

[19] YANG Wen-chao, JI Shou-xun, WANG Ming-pu, LI Zhou, Precipitation behaviour of Al−Zn−Mg−Cu alloy and diffraction analysis from η' precipitates in four variants [J]. Journal of Alloys and Compounds, 2014, 610: 623−629.

[20] SUN Yuan-wei, PAN Qing-lin, LIN Sen, ZHAO Xiang-jin, LIU Zhong-li, LI Wei-jian, WANG Gui-quan. Effects of critical defects on stress corrosion cracking of Al−Zn−Mg−Cu−Zr alloy [J]. Journal of Materials Research and Technology, 2021, 12: 1303−1318.

[21] HUME-ROTHERY W, SMALLMAN R E, HAWORTH C W, The structure of metals and alloys [M]// Metals and Metallurgy Trust of the Institute of Metals and the Institution of Metallurgists. BELGRAVE square, London, 1969.

[22] CHAUBEY A K, MOHAPATRA S, JAYASANKAR K, PRADHAN S K, SATPATI B, SAHAY S S, MISHRA B K, MUKHERJEE P S. Effect of cerium addition on microstructure and mechanical properties of Al−Zn−Mg−Cu alloy [J]. Transactions of the Indian Institute of Metals, 2009, 62(6): 539−543.

[23] WANG Wen-tao, ZHANG Xin-ming, GAO Zhi-guo, JIA Yu-zhen, YE Ling-ying, ZHENG Da-wei, LIU Ling. Influences of Ce addition on the microstructures and mechanical properties of 2519A aluminum alloy plate [J]. Journal of Alloys and Compounds, 2010, 491: 366−371.

[24] LAI Jian-ping, JIANG Rong-piao, LIU Hua-shan, DUN Xiao-long, LI Yan-fen, LI Xiao-qian. Influence of cerium on

microstructures and mechanical properties of Al−Zn−Mg−Cu alloys [J]. Journal of Central South University, 2012, 19: 869−874.
[25] RAMAN K S, DASE S S, VASU K I. Values of solute-vacancy energy in aluminum matrix for Ag, Be, Ce, Dy, Fe, Li, Mn, Nb, Pt, Sb, Si, Y and Yb [J]. Scripta Metallurgica, 1970, 4: 291−294.
[26] LEE S H, JUNG J G, BAIK S I, SEIDMAN D, KIM M S, LEE Y K, EUH K. Precipitation strengthening in naturally aged Al−Zn−Mg−Cu alloy [J]. Materials Science and Engineering A, 2020, 803: 140719.
[27] GAO Xu, ZHAO Yu-tao, KAI Xi-zhou, QIAN Wei, JIN Li-wei, GUAN Chuang, SHENG Peng. Characteristics on microstructure and mechanical performances of 6111Al influenced by Ce-containing precipitates [J]. Journal of Rare Earths, 2022, 40: 153−160.
[28] JIANG Yi-fu, XU Si-yang, GAO Shuang. The effect of initial alloy temper on corrosion resistance for Al−Zn−Mg−Cu alloy [J]. Corrosion Science, 2022, 209: 110730.
[29] GUO Fu-qiang, DUAN Shu-wei, PAN Yu-zhe, WU Dong-ting, MATSUDA Kenji, WANG Tao, ZOU Yong. Stress corrosion behavior and microstructure analysis of Al−Zn−Mg−Cu alloys friction stir welded joints under different aging conditions [J]. Corrosion Science, 2023, 210: 110821.
[30] JIANG Da-ming, LIU Yuan, LIANG Shuai, XIE Wen-long. The effects of non-isothermal aging on the strength and corrosion behavior of Al−Zn−Mg−Cu alloy [J]. Journal of Alloys and Compounds, 2016, 681: 57−65.
[31] GHOSH K S, MUKHOPADHYAY, KONAR B, et al. Study of aging and electrochemical behaviour of Al−Li−Cu−Mg alloys [J]. Materials and Corrosion, 2013, 64: 890−901.
[32] YUAN Ding-ling, CHEN Kang-hua, CHEN Song-yi, ZHOU Liang, CHANG Jiang-yu, HUANG Lan-ping, YI You-ping. Enhancing stress corrosion cracking resistance of low Cu-containing Al−Zn−Mg−Cu alloys by slow quench rate [J]. Materials & Design, 2019, 164: 107558.
[33] MINODA T, YOSHIDA H. Effect of microstructure on intergranular corrosion resistance of 6061 alloy extrusion [J]. Materials Science Forum, 2000, 331−337: 1689−1694.
[34] ZAKARIA S A, ANASYIDA A S, ZUHAILAWATI H, DHINDAW B K, JABIT N A, ISMAIL A. Characterization of mechanical and corrosion properties of cryorolled Al 1100 alloy: Effect of annealing and solution treatment [J]. Transactions of Nonferrous Metals Society of China, 2021, 31: 2949−2961.
[35] WANG Wei-yi, PAN Qing-lin, WANG Xiang-dong, YE Ji, HUANG Zhi-qi, XIANG Sheng-qian, LIU Bing. Effect of laser shock peening on corrosion behaviors of ultra-high strength Al−Zn−Mg−Cu alloys prepared by spray forming and ingot metallurgy [J]. Corrosion Science, 2022, 205: 110458.
[36] XIA Ting-ting, ZENG Long-fei, ZHANG Xue-hui, LIU Jiang, ZHANG Wen-long, LIANG Tong-xiang, YANG Bin. Enhanced corrosion resistance of a Cu−10Ni alloy in a 3.5 wt.% NaCl solution by means of ultrasonic surface rolling treatment [J]. Surface and Coatings Technology, 2019, 363: 390−399.
[37] YANG Ming, LEI Lei, JIANG Yun, XU Fa-hong, YIN Cun-hong. Simultaneously improving tensile properties and stress corrosion cracking resistance of 7075-T6 aluminum alloy by USRP treatment [J]. Corrosion Science, 2023, 218: 111211.
[38] ARGADE G R, KUMAR N, MISHRA R S. Stress corrosion cracking susceptibility of ultrafine grained Al−Mg−Sc alloy [J]. Materials Science and Engineering A, 2013, 565: 80−89.
[39] TSAI T C, CHUANG T H, Atmospheric stress corrosion cracking of a superplastic 7475 aluminum alloy [J]. Metallurgical and Materials Transactions A, 1996, 27: 2617−2627.
[40] MICHALIKA R, WOZNICAB H, The Effect of Ti and REE addition on the corrosion resistance of the AlZn12Mg3.5-Cu2.5 alloy in “Acid Rain” Environment [J]. Solid State Phenomena, 2015, 227: 111−114.

Ce 元素含量对高合金化 Al−Zn−Mg−Cu−Zr−Ti 合金显微组织和耐腐蚀性的影响

李 晨，罗耘天，周青山，韩梦楠，沙少辉，许晓静

江苏大学 先进制造与现代装备技术工程研究院，镇江 212000

摘 要：为了在不影响强度的前提下有效提高铝合金的耐蚀性，研究了 Ce 含量对 Al−11.3Zn−3.1Mg−1.2Cu−0.2Zr−0.1Ti 合金的显微组织，抗应力腐蚀、晶间腐蚀和剥落腐蚀性能的影响。结果表明，Ce 的加入形成了尺寸 100 nm 的$(Zn,Al,Cu)_{22}Ce_3$ 相，提高了合金的再结晶抗力，增加了小角度晶界数量和位错密度，细化了晶粒，促进了合金中 GP 区向 η'相的相变，增加了晶界析出相的尺寸和不连续性。所有添加 Ce 的合金均表现出较强的抗腐蚀性能。添加 0.15% Ce(质量分数)的合金表现出最佳的耐腐蚀性，其在 3.5%氯化钠溶液中的慢速率拉伸强度和伸长率分别为 744.8 MPa 和 4.6%，并获得最小的晶间腐蚀和剥落腐蚀深度。

关键词：Al−Zn−Mg−Cu 合金；微合金化；应力腐蚀开裂；剥落腐蚀；晶间腐蚀

(Edited by Bing YANG)